FULL PAPER

Tandem Solar Cells

ADVANCED
FUNCTIONA
MATERIALS
www.afm-journal.d

Zr-Doped Indium Oxide (IZRO) Transparent Electrodes for Perovskite-Based Tandem Solar Cells

Erkan Aydin,* Michele De Bastiani, Xinbo Yang, Muhammad Sajjad, Faisal Aljamaan, Yury Smirnov, Mohamed Nejib Hedhili, Wenzhu Liu, Thomas G. Allen, Lujia Xu, Emmanuel Van Kerschaver, Monica Morales-Masis, Udo Schwingenschlögl, and Stefaan De Wolf*

Parasitic absorption in transparent electrodes is one of the main roadblocks to enabling power conversion efficiencies (PCEs) for perovskite-based tandem solar cells beyond 30%. To reduce such losses and maximize light coupling, the broadband transparency of such electrodes should be improved, especially at the front of the device. Here, the excellent properties of Zr-doped indium oxide (IZRO) transparent electrodes for such applications, with improved near-infrared (NIR) response, compared to conventional tin-doped indium oxide (ITO) electrodes, are shown. Optimized IZRO films feature a very high electron mobility (up to $\approx$77 cm^2 V^{-1} s^{-1}), enabling highly infrared transparent films with a very low sheet resistance ($\approx$18 Ω $\square^{-1}$ for annealed 100 nm films). For devices, this translates in a parasitic absorption of only $\approx$5% for IZRO within the solar spectrum (250–2500 nm range), to be compared with $\approx$10% for commercial ITO. Fundamentally, it is found that the high conductivity of annealed IZRO films is directly linked to promoted crystallinity of the indium oxide (In$_2$O$_3$) films due to Zr-doping. Overall, on a four-terminal perovskite/silicon tandem device level, an absolute 3.5 mA cm^{-2} short-circuit current improvement in silicon bottom cells is obtained by replacing commercial ITO electrodes with IZRO, resulting in improving the PCE from 23.3% to 26.2%.

1. Introduction

Tandem solar cells are the most straightforward way to exceed the Shockley–Queisser limit of single-junction solar cells.[1] In particular, perovskite/silicon tandems hold great promise for commercialization, now showing 28% PCE on a laboratory scale.[2] Transparent electrodes are essential components in the tandem stack, particularly at their sunward side. Ideally, these electrodes feature simultaneously a high lateral conductivity and broadband transparency to minimize resistive losses and to increase the performance throughout the solar spectrum on device level, respectively. Sputtered transparent conductive oxides (TCOs) are the first choice for transparent electrodes since they fulfill relatively well the seemingly contradictive transparency/conductivity requirements. In addition, TCOs can be processed at a low temperature and with proven industrial scalability. In perovskite-based tandems, the perovskite top cell should efficiently harvest the blue part of the solar spectrum whereas the bottom cell, which can be silicon, copper–indium–gallium–selenide, or another metal halide perovskite do so for the near-infrared part.[3,4] Importantly, the top cell should also be highly NIR transparent. For perovskite absorbers, this requirement is fulfilled by their steep absorption edge and absence of deep optical states.[5] Based on these arguments, for highly efficient devices, it is critical that the transparent electrodes should combine a wide bandgap with minimal free-carrier absorption (FCA), to avoid parasitic absorption in the blue and red parts of the solar spectrum, respectively. Losses associated with FCA can be reduced by decreasing the carrier density of the transparent electrode.[6] However, to maintain a low sheet resistivity, strategies to increase carrier mobility are then required. Motivated by these criteria, some TCOs based on doped In$_2$O$_3$ have already been explored in literature for tandem solar cells such as ITO, Zn-doped In$_2$O$_3$ (IZO), and ITO/H-doped In$_2$O$_3$ (In$_2$O$_3$:H) bilayer electrodes.[4,7] In this, ITO, whereas being well established, is of limited appeal because of its low mobility

**ADVANCED
SCIENCE NEWS**
www.advancedsciencenews.com

**ADVANCED
FUNCTIONAL
MATERIALS**
www.afm-journal.de

due to the ionized impurities and high parasitic absorption, especially in the NIR range.[8] Conversely, crystalline In_2O_3:H has a very high mobility and optical transparency.[9] Unfortunately, this TCO may degrade the device performance due to water vapor effusion.[10] IZO, which is another promising TCO, enables a mobility of ≈60 cm^2 V^{-1} s^{-1} without the need of post-annealing.[11] However, due to its amorphous nature, its band edge is "blurry," causing parasitic absorption in the blue part of the spectra.[11] Alternatively, other transition metals such as Ti, Ce, W, Mo can also be used for heteroatom doping of In_2O_3. However, such dopants have not been explored widely in tandem solar cells because of high-temperature annealing requirements to activate these materials.[12] Recently, IZRO has been explored as a high-mobility and NIR transparent TCO, resulting in improved short circuit current density (J_{SC}), compared to conventional TCOs in silicon heterojunction (SHJ) solar cells.[13] Excellent optoelectronic properties such as high transparency, wide bandgap (>3.5 eV), and high conductivity, combined with high NIR transparency make IZRO a promising electrode for perovskite single junction and perovskite-based tandem solar cells.

In this study, we thoroughly studied the structural and optoelectronic properties of radio frequency (RF) sputtered IZRO films, using 2 wt% zirconium oxide (ZrO_2)-doped In_2O_3 targets. This doping ratio has already been successfully proven to obtain maximum conductivity for In_2O_3.[6,13,14] Here, we investigated critical processing parameters for application in perovskite solar cells (PSCs), such as process pressure, oxygen partial pressure $r(O_2)$, and film thickness for as-deposited and annealed (at 200 °C in ambient air) samples, aiming at gentle deposition on the soft perovskite thin films. Finally, we tested our IZRO electrodes in four-terminal perovskite/silicon tandem solar cells.
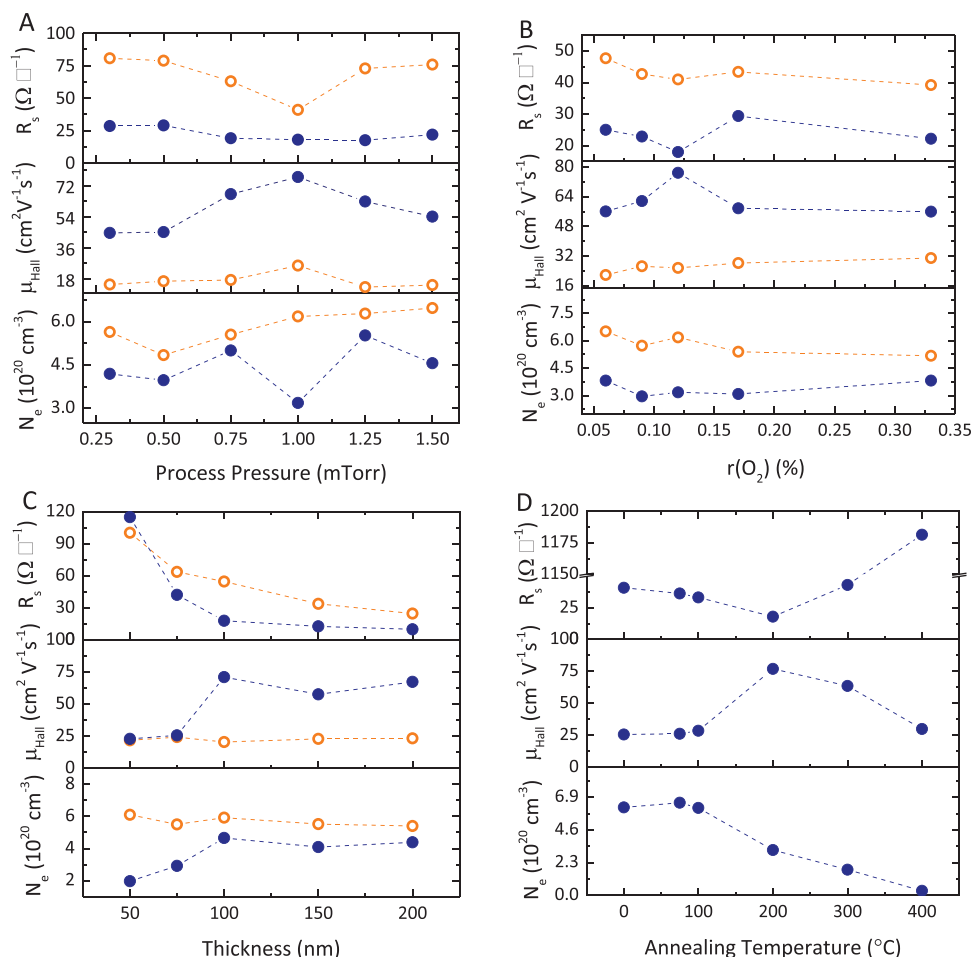
2. Results and Discussion

We developed our IZRO electrodes by targeting high conductivity and transparency by using low power densities, and room temperature depositions to avoid damaging the underlying soft layers. Table S1 in the Supporting Information summarizes the results for tested process parameters. We found that as-deposited films processed at a total process pressure [$r(O_2)$ +$r(Ar)$] of 1 mTorr, with $r(O_2)$ = 0.12% give the highest mobility and lowest sheet resistance (**Figure 1**a) as well as excellent optical transparency (Figure S1a,b, Supporting Information). Next, we studied the role of the thickness of IZRO films and found that increased film thickness yields a decrease in sheet resistance (Figure 1c) and optical transparency (Figure S1e,f, Supporting Information) for as-deposited as well as annealed samples. When the film thickness reached 100 nm, the electron density (N_e) and mobility (μ_e) remained in a similar range compared to thinner films. For films post-annealing at temperatures lower than 200 °C, no substantial changes are found in the structural and electronic parameters. However, above 200 °C, the resistivity increases drastically, as summarized in Table S1, Supporting Information. We correlate this to an amorphous-to-crystalline phase transition, occurring at 200 °C, as apparent from X-ray diffraction (XRD) spectra, shown in **Figure 2**c. For the samples

post-annealed at 200 °C, we obtained the combination of the lowest sheet resistivity (18 Ω ☐$^{-1}$, with μ_e = 77 cm^2 V^{-1} s^{-1}, Table S1, Supporting Information) with the highest optical transparency (Figure 4a). The increased carrier concentration after annealing at 200 °C can be attributed to enhanced Zr^{4+} ion doping activation.[6] Here, Zr acts as a shallow donor via substituting In^{3+} by Zr^{4+} (generating one electron per Zr atom), making the In_2O_3 degenerately doped.[6] Further increasing the temperature resulted in a decrease in free-carrier density, and thus decreased conductivity, probably because of further oxidation. It is worth noting that annealing of IZRO at 200 °C in an inert atmosphere (nitrogen filled glove box, <0.1 ppm O_2 and H_2O) resulted in similar optoelectronic properties, which indicates that ambient-specific annealing is not a requisite.

Figure 2c shows the XRD patterns of the as-deposited and annealed (at 200 °C) IZRO films. As-deposited films show an amorphous nature without characteristic reflections; crystallization and grain growth become notable when samples are post-annealed above 200 °C. However, further increasing the annealing temperature did not increase the crystallinity which can be witnessed from the XRD spectra given in Figure S3 in the Supporting Information. Based on these results, it appears that annealing at 200 °C for 25 min suffices to obtain fully crystalline films (no remnants of amorphous tissue) as also suggested by the top-view scanning electron microscope (SEM) images in Figure 2b. After post-annealing, IZRO films showed a preferred orientation in growth to the (400) plane, characteristic of the unit cell of cubic In_2O_3 (PDF 01-071-2194). The 2θ positions of the detected peaks and assigned crystallographic planes are listed in Table S3 in the Supporting Information together with PDF data. Most of the peaks show a small shift toward higher angles which may be correlated with the presence of interstitial Zr atoms in the lattice; substitutional Zr doping is not likely to cause stress to the lattice due to the similar atomic radii of In^{3+} (80 pm) and Zr^{4+} (72 pm).[6] The absence of peaks originating from impurity phases may indicate the formation of a solid solution with Zr-doping.

In agreement with the XRD analysis, SEM top-view images revealed that as-deposited films are mainly amorphous, and after annealing at 200 °C for 25 min the films become crystalline (Figure 2b). This behavior is similar to that of nondoped and Zr-doped In_2O_3 films (Figure S4, Supporting Information). The XRD spectra also confirm the increased crystallinity of the films compared to their nondoped counterparts by showing an increased intensity of the main peak (Figure S5, Supporting Information). These results indicate that Zr doping of the In_2O_3 films notably promotes the formation of larger grains, compared to the nondoped films (see also SEM images in Figure S4, Supporting Information). A similar annealing behavior was earlier reported for H doping of In_2O_3.[15] Following the Scherrer formula, we calculated the average crystal size in IZRO films as 105 nm, to be compared with 47 nm for a nondoped sample.[16] This remarkable improvement in crystal size arguably helps IZRO films to have higher mobility and conductivity. Indeed, earlier, Koida et al. correlated the increased mobility of In_2O_3:H films with a longer optical relaxation time, rather than with a smaller effective electron mass in the crystallized films (as compared with the as-deposited films).[15]

ADVANCED
SCIENCE NEWS
www.advancedsciencenews.com

ADVANCED
FUNCTIONAL
MATERIALS
www.afm-journal.de

Figure 1. The change of sheet resistance (R_S), Hall mobility (μ_{Hall}), and free-carrier concentration (N_e) as a function of a) process pressure ($r(O_2) + r(Ar)$), b) $r(O_2)$ in plasma gas mixture, c) thickness of the films, and d) post-annealing temperature of IZRO films. Open circles (o) show the as-deposited while closed circles (•) show annealed samples at 200 °C (except for annealing temperature part), d). Whereas the influence of process pressure has been studied with $r(O_2) = 0.09\%$ and 100 nm films, the $r(O_2)$ has been studied for 1 mTorr optimized process pressure. The thickness of the films has been studied for 1 mTorr process pressure and $r(O_2) = 0.12\%$. Post-annealing of the films has been performed for 100 nm films processed at 1 mTorr process pressure and $r(O_2) = 0.12\%$.

To further elucidate the effect of annealing on the conductivity and electron transport properties of IZRO films, we performed temperature-dependent Hall-effect measurements in a range from 300 K down to 10 K (Figure 2d). For this, as-deposited (amorphous) and annealed (crystalline) IZRO films were compared. For both films, N_e is independent of temperature as expected for degenerate semiconductors. Regarding the electron mobility, the amorphous film shows only a relative change of 13% with cooling down, while the crystalline film shows a relative change of 33% (reaching 115 cm² V⁻¹ s⁻¹ at 10 K). Temperature-dependent Hall-effect measurements were performed using a Quantum Design Physical Measurement System (PPMS) and $\mu_{e,annealed}$ was found 87 cm² V⁻¹ s⁻¹ at room temperature, which is slightly higher than the results obtained with a Lake–Shore system. For the as-deposited IZRO film, the weak dependence of μ_e with temperature is indicative of transport dominated by ionized or neutral impurity scattering, as observed for several doped amorphous oxides.[17] Contrary to this, for the crystalline sample, the increment in μ_e with cooling down from 300 to 100 K is indicative of lattice

(phonon) scattering. Sources of lattice scattering can arise from optical and/or acoustic phonons. Polar optical phonon scattering has been generally proposed as the main contributor to phonon scattering in In_2O_3.[18,19] Using the approximation for polar optical phonon scattering, $\mu \propto T^{-p}$, we determined $0.24 < p \leq 0.45$ for the annealed IZRO sample (Figure 2d). This is lower than the $p = 2.2$ reported for unintentionally doped epitaxially grown In_2O_3 films.[19] The small slope for our polycrystalline IZRO suggests that although photon scattering dominates, ionized impurities and/or grain boundaries still contribute to the scattering of carriers in the IZRO films.

Next, we verified the Zr content of the films by energy dispersive spectroscopy (EDS) analysis. EDS spectra shown in Figure S6 in the Supporting Information reveal that as-deposited films contain 1.4 at.% Zr, similar to annealed films with 1.6 at.%. The Zr concentration in thin films is slightly lower than the target composition, which is expected for sputtered films from doped targets since different metals have different energy distributions of sputtered atoms. Additionally, the O/In ratio increased by annealing, which confirms the

higher O intake due to the oxidization of Zr^{4+} or O vacancies. The EDS analysis also revealed that the white spots observed on the films have the same elemental composition as the rest of the films for both doped and nondoped films (Figure S6c, Supporting Information). We believe therefore that these regions are the seeding points for the crystal growth during the post-annealing.

To further understand the effect of Zr doping, we performed density functional theory (DFT) calculations on a bixbyite In_2O_3 lattice system. We obtain a lattice parameter of 10.30 Å, which is 1.7% higher than the previously reported experimental value.[20] In order to study Zr doping, we replaced one of the 32 In atoms with Zr such that the doping concentration is 3.125%, finding that the lattice constant slightly expands to 10.31 Å. The crystal structure of IZRO is shown in Figure 2a. The formation energy of Zr substitution is calculated as $E_{FE} = E_{IZO} - (E_{IO} + \mu_{In} + \mu_{Zr}) = 4.89$ eV, where E_{IZO} and E_{IO} are the total energies of the Zr-doped and pristine In_2O_3 crystals, respectively, and μ_{In} and μ_{Zr} are the chemical potentials of In and Zr obtained from their bulk phases. Usually, the chemical potentials depend on the growth conditions. We calculated the bandgap to be 0.92 eV for In_2O_3. This is in agreement with a previously reported DFT value of 0.90 eV,[21] but notably underestimates—as expected for DFT[22]—the experimental

value of ≥2.7 eV for a single crystal.[23] From the partial density of states (Figure S10, Supporting Information), the valence band maximum (VBM) is found to be primarily due to O (p) states, but also includes contributions of In (p and d) states. The conduction band minimum (CBM) is due to hybridized In (s) and O (p) states, and we found that the addition of Zr does not cause hybridization with these CBM states. Similar behavior has been found for Ce doping in In_2O_3.[24] Since the dispersion of the CBM does not change by Zr substitution, we attribute the increment in the measured electron mobility to the enhanced grain size.

We performed the X-ray photoelectron spectroscopy (XPS) to characterize the chemical composition of the IZRO films and to determine the oxidation state of Zr. Survey spectra proved the presence of In, O, Zr, and C elements in the structure before and after annealing of the films (**Figure 3**c). The determined Zr/In atomic ratio from the XPS survey spectrum was found to be equal to 0.01 in consistent with EDS results. Figure 3d displays high-resolution XPS spectra of the In 3d core level for the samples. This level shows two peaks corresponding to In $3d_{5/2}$–In $3d_{3/2}$ doublet located at 444.6 and 452.2 eV, respectively, characteristic of In_2O_3.[25] No significant changes were observed comparing as-deposited and annealed samples. High-resolution XPS spectra of O 1s core level of both as-deposited and
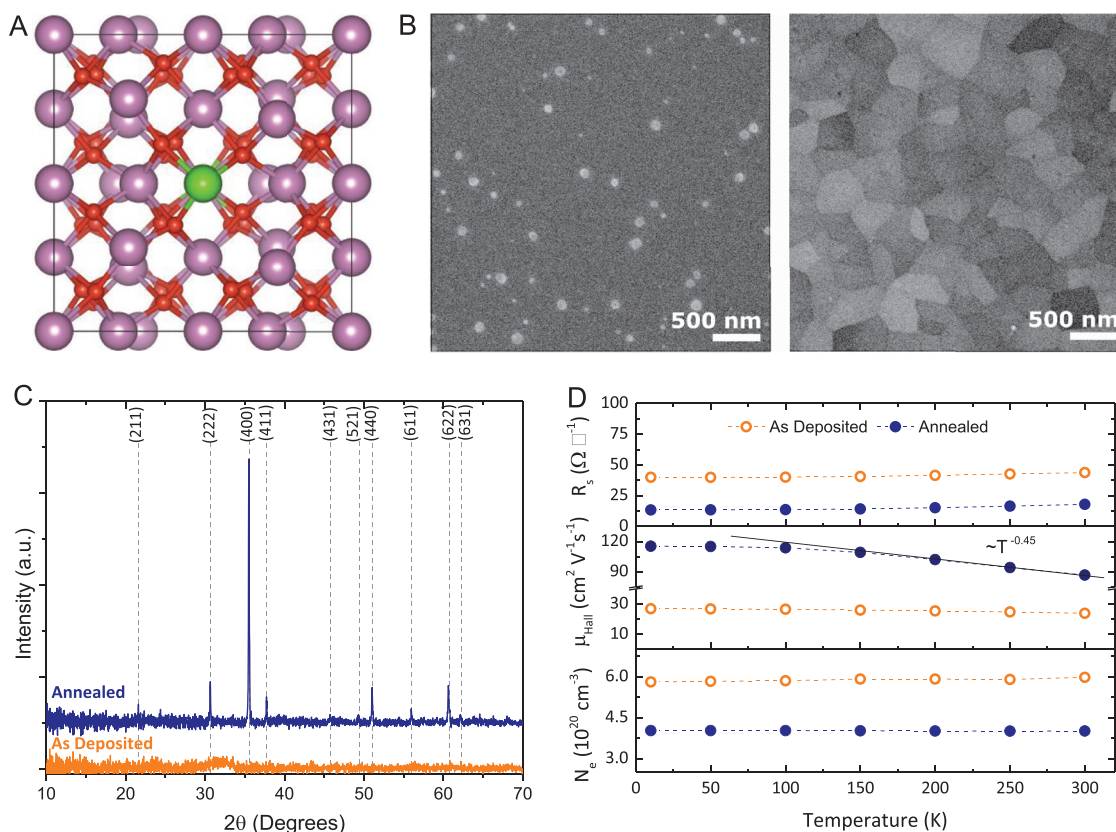
Figure 2. a) Crystal structure of In_2O_3 crystal with Zr substitution of In atoms. Pink, red, and green colors represent In, O, and Zr atoms, respectively. b) SEM top view of the IZRO films before and after the annealing process showing the formation of large crystals after annealing at 200 °C explicitly. c) XRD spectra of the IZRO films before and after annealing confirming the phase transition from amorphous to crystalline. d) Temperature-dependent Hall-effect measurements for as-deposited and annealed samples between 10 and 300 K. The thin straight line qualitatively represent asymptotic mobility due to polar optical phonon scattering only.
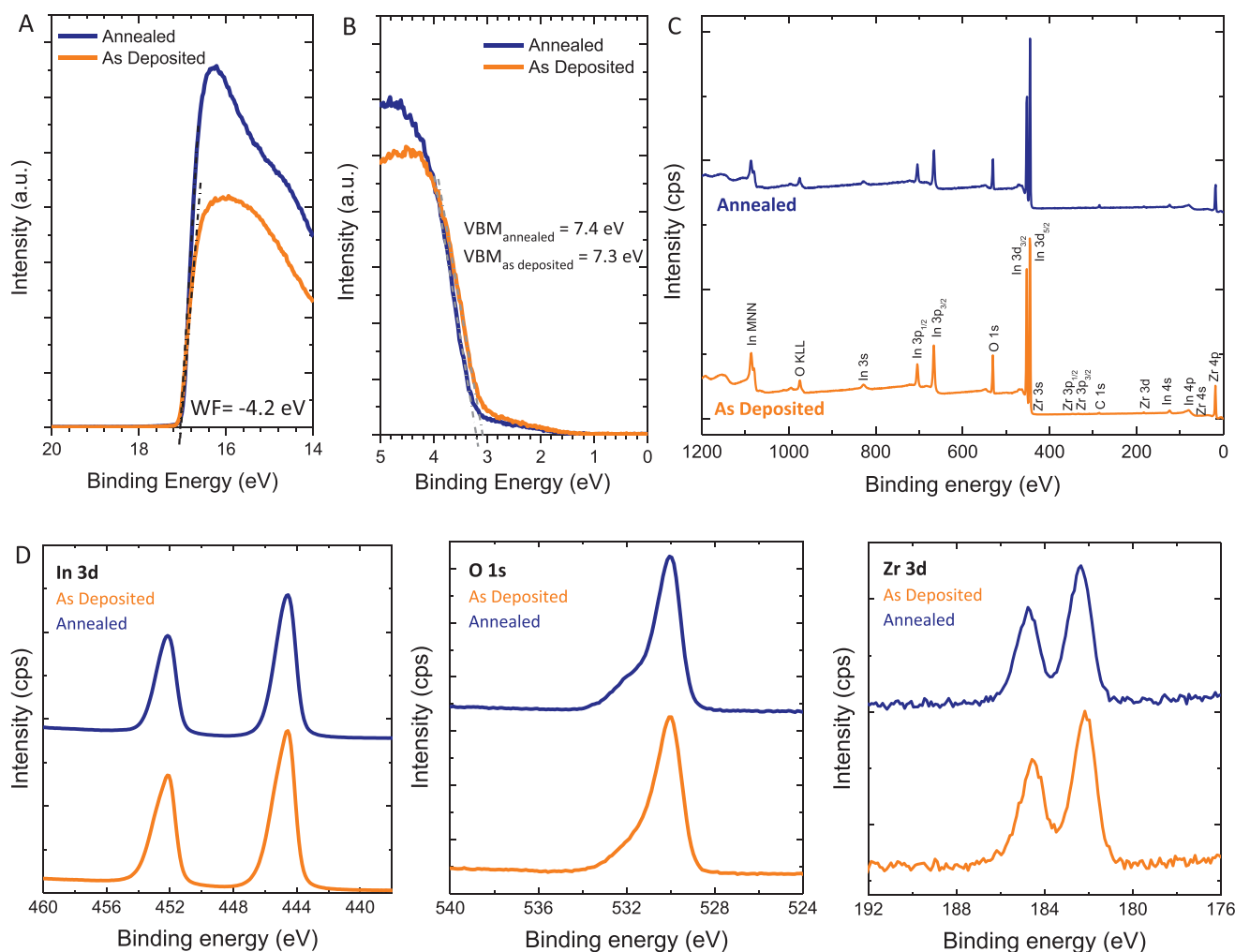
Figure 3. UPS spectra showing the a) work funcion (WF) and b) valance band maximum (VBM) values. c) XPS survey of the IZRO films before and after the annealing process. WF values have been calculated by $WF = 21.2 - WF_{cutoff}$ (eV). VBM values have been calculated by $VBM = WF + VBM_{cutoff}$. d) Detailed view on XPS spectra of In 3d, O 1s, and Zr 3d states with direct comparison of as-deposited and annealed samples.

annealed IZRO show a peak located at 530.0 eV with a shoulder at high binding energy around 531.8 eV (Figure 3d). The dominant peak at 530.0 eV corresponds to the oxygen bond of In—O—In, the small peak situated at higher binding energy 531.8 eV refers to a combination of hydroxide and oxygen defects in the matrix of metal oxide and organic oxygen.[25] Previously, this peak was reported to disappear by annealing of In_2O_3:H films.[26] The high-resolution XPS spectra of Zr 3d core level for the as-deposited sample show two characteristic peaks of ZrO_2 corresponding to Zr $3d_{5/2}$–Zr $3d_{3/2}$ located at 182.2 and 184.8 eV, respectively (Figure 3d).[27] After annealing, we observed a small shift of about 0.2 eV to higher binding energy, which can be attributed to further oxidation of Zr.

The work function (WF) of IZRO films is another important parameter to be considered for device engineering. Here, we obtained a WF of −4.2 eV from ultraviolet photoelectron spectroscopy (UPS) for both as-deposited and annealed IZRO films (Figure 3a). The measured values are very close to the previously reported WF of −4.3 eV for thick In_2O_3 films.[28] We measured the WF of the nondoped In_2O_3 films, which are

deposited with the same process parameters, to be −4.1 eV for both as-deposited and annealed samples, which can be seen in Figure S4 in the Supporting Information. We also performed DFT calculations for the WF of O terminated (12 O atoms on each surface) and In terminated (eight In atoms on each surface) In_2O_3(100) slabs by using the expression $WF = E_v − E_F$, where E_v and E_F are the vacuum and Fermi energies, respectively. The WF of pure In_2O_3 is −7.51 eV for O-termination, decreasing to −6.85 eV when the surface oxidation is reduced (six O atoms on each surface). Termination by In gives a WF of −4.60 eV and −4.38 eV for pure and Zr-doped In_2O_3, respectively, which is very close to experimental values. Experimental results confirmed the WF to be −4.2 eV (undoped −4.1 eV). This opposing behavior might be related to the dependency of the ionization potential and WF of In_2O_3 on the surface orientation.[29]

Compared to standard ITO, IZRO electrodes provide better transparency in the high energy part of the solar spectrum. **Figure 4**a shows the transmittance and absorptance of the films measured by UV-vis–NIR spectroscopy, revealing that the
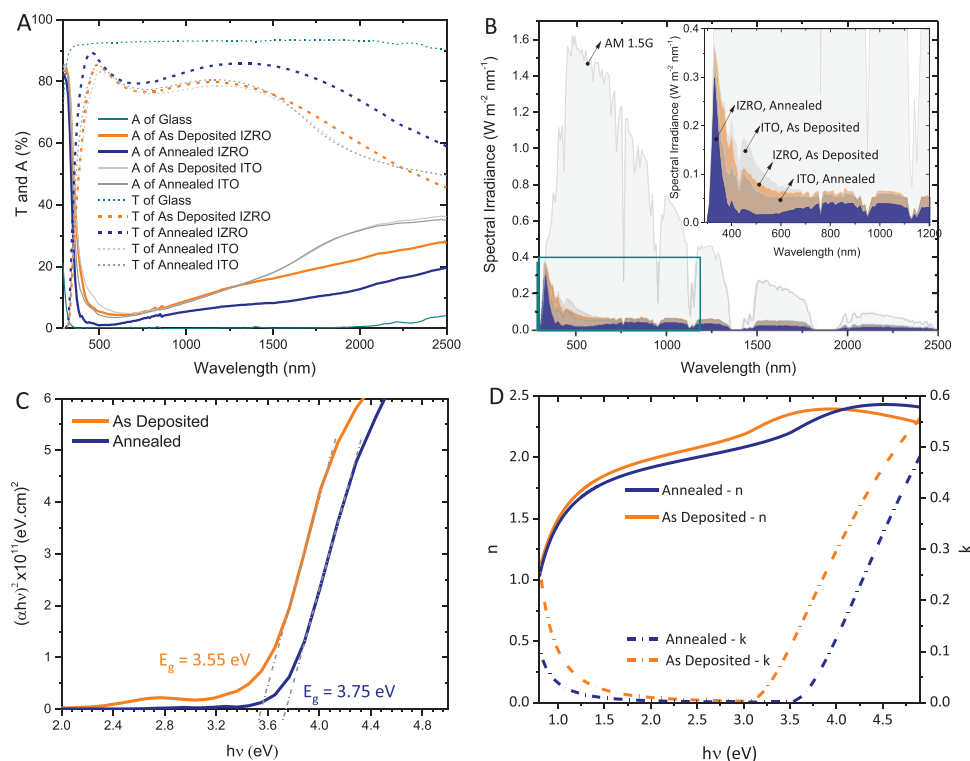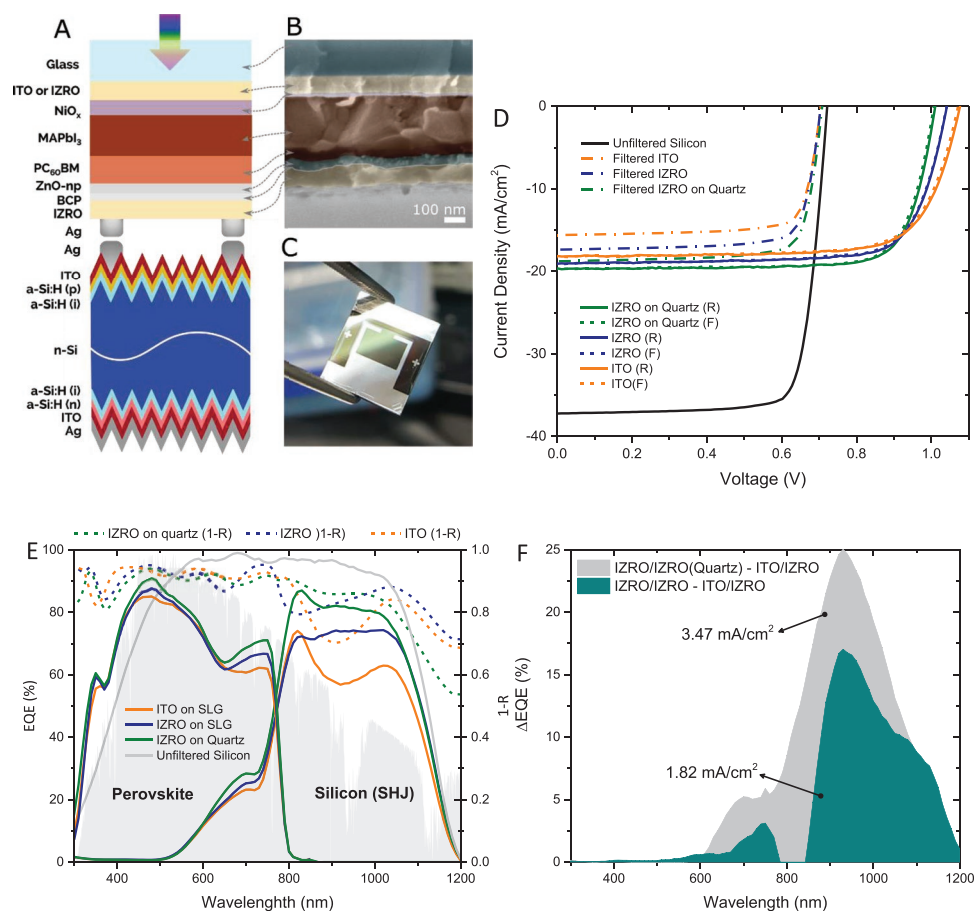
Figure 4. a) Transmittance (*T*) and absorptance (*A*) and b) solar-weighted absorbance spectra of the sputtered IZRO and ITO films measured with integrating sphere. The shaded area shows the spectral irradiance for AM 1.5 conditions. c) The optical bandgap values of the IZRO from $(\alpha h\nu)^2$ versus $h\nu$ graph. d) Refractive index (*n*) and extinction coefficient (*k*) for as-deposited and annealed IZRO films.

transparency of the films increases drastically by annealing, whereas the transparency of ITO changes only slightly. We correlate this improvement with increased crystallinity and decreased N_e, where the former also leads to improved carrier mobility. Solar-weighted absorptance plots indicate that while as-deposited IZRO absorbs 98.3 mW cm^{-2} ($\approx$10%) of the solar spectrum, annealed IZRO films absorb only 48.9 mW cm^{-2} ($\approx$5%) (Figure 4b). Contrasting with this, as-deposited ITO film absorbed 111.9 mW cm^{-2} ($\approx$12%) and annealed ITO 93.8 mW cm^{-2} ($\approx$10%). This underlines the great potential of IZRO to reduce the parasitic absorption losses in solar cells and hence improve their power output, especially for annealed samples. We calculated the optical bandgap values of the films by the extrapolation of the linear region of the $(\alpha h\nu)^2$ versus $h\nu$ graph as shown in Figure 4c.[30] Accordingly, whereas as-deposited films have a 3.55 eV bandgap, by annealing this value shifted to 3.75 eV; such broadening of the bandgap is often observed for wide bandgap TCOs.[13,31] DFT calculations revealed that Zr-doping enlarges the bandgap to 1.01 eV from 0.92 eV, suggesting that increased bandgap of the films might be due to the combined effect of promoted crystallinity and the Moss–Burstein shift observed for doped In$_2$O$_3$ films.[13]

The refractive index (*n*) and extinction coefficient (*k*) are widely used optical parameters to understand the absorption losses and light in-coupling on the device level. The dependency of *n* and *k* values on the photon energy ($h\nu$) of the as-deposited and annealed IZRO films are shown in Figure 4d which were extracted from measured spectroscopic ellipsometry (SE) data.

At short and long wavelengths, the *k* values decrease, and the absorption edge blue shifts. The improvement in short wavelengths can be attributed mainly to the improved crystallinity of the IZRO films after annealing whereas the improvement in the long wavelengths might be assigned to a decreased carrier density and thus FCA.[32] Thanks to decreased FCA, parasitic absorption losses reduced which can be translated in improved light coupling of the NIR part of the spectrum in solar cells.

Subsequently, we tested the performance of the IZRO electrodes in four-terminal perovskite/silicon tandem solar cells. We fabricated semitransparent PSCs with the structure of NiO$_x$/MAPbI$_3$/PC$_{60}$BM/ZnO/BCP/IZRO/Ag on either ITO or IZRO transparent electrodes (**Figure 5**a). For the low bandgap bottom cell, we used an n-type SHJ solar cell, which characteristically features a high V_{OC}.[33] Figure 5b,c shows the cross-sectional SEM image of the stacked layers and the photograph of the fabricated semitransparent PSCs, respectively. First, we compared the semitransparent solar cell performance of ITO and IZRO front electrodes by keeping the IZRO back electrode in all cases. We found that, while ITO front electrode-based devices were giving 1078 mV V_{OC}, IZRO-based devices feature a V_{OC} of 1042 mV on the soda-lime glass and 1008 mV on quartz substrates (**Table 1** and Figure 5). The V_{OC} difference between ITO- and IZRO-based devices might be attributed to the band alignment of the electrodes as UPS analysis revealed that the WF of the IZRO films is −4.2 eV while ITO has −4.7 eV. The difference for the film deposited on soda-lime glass and quartz substrates might be related to substrate-specific film-growth

**ADVANCED
SCIENCE NEWS**
www.advancedsciencenews.com

**ADVANCED
FUNCTIONAL
MATERIALS**
www.afm-journal.de

Figure 5. a) Schematics of the fabricated semitransparent perovskite top cells and c-Si bottom cells. b) Stacked layers of IZRO/NiO$_x$/MAPbI$_3$/PC$_{60}$BM/ ZnO-np/IZRO structure imaged by cross-sectional SEM analysis c) together with the photograph of the regarding devices. d) J–V graphs and e) EQE spectra of the mechanically stacked perovskite/silicon tandem solar cells and individual top and bottom cells with 0.16 cm² top cell aperture area and 4.2 cm² bottom cell area, respectively. All measurements were done without any antireflection coating and foil. The shaded area shows the AM 1.5G spectra. f) Δ_{EQE} = EQE$_{IZRO}$ − EQE$_{ITO}$ for both soda-lime and quartz glass substrates which is showing absolute current gain on SHJ bottom cells.

Table 1. Performance overview for the silicon solar cells, NIR transparent solar cells, and mechanically stacked solar cells. Note that silicon solar cells are measured over 4.2 cm² aperture area while semitransparent solar cells over 0.16 cm². Four-terminal tandem solar cells are measured over 4.2 cm² aperture area by using full area perovskite devices as a filter on 1 in.² glass substrates. IZRO back electrode is common for all semitransparent devices and these electrodes were used without any thermal treatment. No antireflection foils or layer has been utilized for the J–V measurements.

Devices	V_{oc} [mV]	J_{sc} [mA cm⁻²]	FF [%]	PCE [%]
c-Si	722	37.2	79.7	21.4
Filtered c-Si (ITO based)	704	15.6	79.2	8.7
Filtered c-Si (IZRO based)	704	17.4	79.0	9.7
Filtered c-Si (IZRO on quartz based)	708	18.8	79.3	10.6
Semitransparent PSC (ITO based)	1078	18.2	74.0	14.6
Semitransparent PSC (IZRO based)	1042	19.1	76.0	15.1
Semitransparent PSC (IZRO on quartz based)	1008	19.8	78.0	15.6
4T-Tandem (ITO based)	–	–	–	23.3
4T-Tandem (IZRO based)	–	–	–	24.8
4T-Tandem (IZRO on quartz based)	–	–	–	26.2

dynamics. We found that IZRO-based semitransparent PSCs showed 0.9 mA cm⁻² current gain respect to ITO-based devices. Thanks to the improved NIR transparency by IZRO electrodes compared to ITO, a 1.8 mA cm⁻² current gain was obtained on filtered c-Si bottom cells (Figure 5e). This difference became more notable when we used quartz substrates instead of soda-lime glass as can be seen in Figure 5f. Δ_{EQE} = EQE$_{IZRO}$ − EQE$_{ITO}$ analysis confirmed that IZRO electrodes enable improved light harvesting. Overall, across the whole absorption spectrum, we achieved an absolute current gain of 3.5 mA cm⁻² (using quartz substrates) compared to ITO-based electrodes, and four-terminal tandem PCE reached to 26.2% which is comparable with other reported efficient devices.[34] Importantly, 1-R plots show that employing IZRO electrodes enables an improved spectral response

**ADVANCED
SCIENCE NEWS**

www.advancedsciencenews.com

**ADVANCED
FUNCTIONAL
MATERIALS**

www.afm-journal.de

thanks to reduced reflection losses (Figure 5e). To verify the improved NIR response of the tandem solar cells, we compared the results with c-Si solar cells with electron-selective titanium dioxide (TiO_2) rear contact, which gives an excellent external quantum efficiency (EQE) response in both short and long wavelength range and high PCE (22.1%).[35] We found that such devices provide 2.3 mA cm^{-2} absolute current gain and overall four-terminal tandem PCE is 24.8% which is slightly lower than SHJ cells (Figure S14, Supporting Information). Herein, SHJ cells get benefit of their high V_{OC} and better NIR response although they suffer from a somewhat moderate UV response originating from parasitic absorption at the front contact stack.[36] Achieved PCE results highlight also the key role of the high V_{OC} of the silicon bottom cells to achieve high-efficiency tandems. Overall, these results revealed the full potential of IZRO electrodes on tandem solar cells by proving the improved light harvesting.

3. Conclusion

In summary, we successfully implemented IZRO films as front and rear transparent electrodes on perovskite semitransparent solar cells for tandem applications, using low power density and low thermal budget to protect underlying soft layers. Our IZRO electrodes showed improved transparency and low sheet resistance (41 and 18 Ω □$^{-1}$ for as-deposited and annealed films, respectively) which are encouraging to increase the finger spacing on the tandem solar cells, essential to increase the current in devices. Beyond this, the high conductivity of the IZRO films may help to decrease the thickness of the transparent electrodes, which directly translates in less indium usage. In the long term, this might help to decrease the price of the tandem solar cells. Besides, we foresee that IZRO can replace ITO as a recombination junction in monolithic tandem solar cells to improve the NIR response of the silicon bottom cells. Moreover, here we engineered IZRO films with a low thermal budget, which means such electrodes can be used on different low-temperature resilience substrates and device structures as well. Finally, IZRO electrodes may find applications in other electronic devices beyond silicon and perovskite-based solar cells, such as IR-sensitive quantum dot solar cells, thin film transistors, and organic light-emitting diodes.

4. Experimental Section

Deposition of IZRO Films: IZRO films were grown on soda-lime glass substrates by RF sputtering technique (Angstrom Engineering). As a target material, 98 wt% In_2O_3 and 2 wt% ZrO_2 were used. Argon and 2.5% oxygen/argon gas mixture were used as a process gas. It is of note that no water was intentionally introduced to the system and base pressure was kept <5 × 10^{-7} Torr before the deposition to eliminate the contribution of the water during the processing. The deposition rate of the optimized IZRO films was 0.21 Å s^{-1}. All depositions were performed at room temperature without any intentional heating. The gas flow ratio, process pressure, and the thickness of the layers were engineered as defined in the main text.

Fabrication of Semitransparent Perovskite Solar Cell: First, NiO$_x$ layers were deposited on the precleaned commercial ITO-coated (Xin Yan Technologies, 15 Ω □$^{-1}$) or homemade IZRO-coated glass substrates via RF magnetron sputtering technique at room temperature and with high uniformity over large area as reported previously.[37] Perovskite precursor was prepared by dissolving 507 mg PbI$_2$ (TCI) and 175 mg methylammonium iodide (Greatcell Solar) in 970 μL *N*,*N*-dimethylformamide and 75 μL dimethyl sulfoxide (both Sigma Aldrich). This precursor was dropped onto the substrate's NiO$_x$ surface, and the spin process was started (4000 rpm for 30 s). Then, 24 s before the end of the spin cycle (in other words, after 6 s), 100 μL chlorobenzene (Sigma Aldrich) was pipetted onto the spinning substrate. Samples were annealed in a nitrogen-filled glovebox at 100 °C for 10 min before cooling to room temperature. Next, a 20 mg mL^{-1} solution of PC$_{60}$BM (>99.5%, Lumtec) in anhydrous chlorobenzene was spin casted onto the perovskite films at 1300 rpm for 30 s. As a buffer layer, ZnO nanoparticle solution (Avantama) was spin cast on PC$_{60}$BM layer as defined previously without any annealing step.[38] Finally, an ultra-thin layer of bathocuproine (Sigma Aldrich) cathode modification layer was spin casted at 5000 rpm for 10 s from a 0.5 mg mL^{-1} solution in anhydrous ethanol. 100 nm IZRO (41 Ω □$^{-1}$) was deposited by RF sputtering as transparent electrode. Devices were completed by the thermal evaporation of a 100 nm thick silver contact at 10^{-6} mTorr.

Fabrication of the TiO$_2$ Passivated Silicon Bottom Cell: The bottom silicon cell (4.2 cm^2), featuring a high-performance full-area SiO$_2$/TiO$_2$ electron-selective contact at the rear side, was fabricated on n-type FZ-Si wafers (1.0 Ω cm). The textured front side with random pyramids had a boron-diffused p^+ emitter, passivated by Al$_2$O$_3$/SiN$_x$ stack. The front fingers (≈30 μm) were prepared by thermal evaporation of a Cr/Pd/Ag seed layer and subsequently thickened by silver electroplating. The fabrication details were reported previously.[35,39]

Fabrication of the n-Type SHJ Bottom Cell: 250–280 μm thick float-zone double-side-polished 4 in. wafers (n-type, resistivity 1–5 Ω cm) were used to fabricate SHJ cells. Texturing was performed by concentrated KOH solution. After the texturing process, the wafers were rinsed three times in a dedicated deionized water bath and finished with the RCA cleaning process. The wafers were passivated and carrier-selective contacts were created by deposition of intrinsic and doped hydrogenated amorphous silicon layers. The cells were then finished with ITO deposition and metallization with full-area silver on the rear-side and screen-printed silver grid on the front side.

Solar Cell Measurements: *J*–*V* characteristics of the semitransparent PSCs were characterized using a custom-made temperature-controlled jig as defined in previous studies.[40] To avoid back reflections to semitransparent PSCs, the back side of the jig was mate black painted. All devices were tested under 1-sun illumination conditions (100 mW cm^{-2}, AM 1.5G, 25 °C) employing Wavelabs LED-based solar simulator which was calibrated by Fraunhofer-certified c-Si calibration cell. Semitransparent devices had 0.16 cm^2 aperture area. Note that the reverse scan was from V_{OC} to J_{SC} (1.2 V → − 0.1 V), and the forward scan was from J_{SC} to V_{OC} (− 0.1 V → 1.2 V). No preconditioning protocol was used before the measurement. Silicon solar cells were measured with a scan rate of 1.4 V s^{-1}. For four-terminal tandem measurements, the bottom cell was measured by using the perovskite top cell (without metal contacts) as a filter by illuminating from the glass side. No antireflection layer and foil was employed.

EQE Measurements: The EQE spectra of our perovskite cells were measured with a commercial EQE system (Newport) equipped with a xenon lamp and under dark conditions and without any biasing and preconditioning. Semitransparent solar cells were illuminated from the glass side. The c-Si bottom cell was filtered by semitransparent solar cells during the EQE measurements. EQE of the c-Si bottom cells was measured by focusing the beam between two metal fingers. The calibration of the EQE tools was performed by a silicon and germanium diodes.

Characterization—Hall Effect: Room temperature Hall-effect measurements were performed on Lake–Shore Hall-effect system at dark conditions. Samples were prepared in Van der Pauw geometry. Connections of silver wires for the electrical measurements were made by conductive silver paste. After drying process of the paste, the ohmic behavior of the metal contacts was checked by the linear

variation of the current–voltage (I–V) characteristics which was observed to be independent of the polarity of the applied current and the contact combinations for each sample. Measurements were done under 10 kG magnetic field. The sample size was 10×10 mm². Temperature-dependent Hall-effect measurements were performed using a PPMS in the temperature range of 10–300 K at a current level of 10 μA and magnetic field of ± 9 Tesla. Sample preparation was identical to the one described for room temperature Hall-effect measurement.

Characterization—SEM-EDX: Surface and cross-sectional images of the samples were taken by a Carl Zeiss AURIGA CrossBeam Workstation using in-lens detectors. A 5 kV voltage was used to accelerate the electrons, and the working distance was 5 mm. Energy-dispersive X-ray spectroscopy analysis was performed at 10 keV accelerating voltage using Oxford X-max 20 detector under a pressure of typically 10^{-9} mBar.

Characterization—Transmittance/Reflectance: A PerkinElmer Lambda 950 UV-vis–NIR spectrophotometer was used to investigate the transmittance of samples between 200 and 2500 nm range with the integrating sphere. Absorptance of the films was calculated by $A = 100 - (T + R)$ method.

XPS and UPS Measurements: XPS studies were carried out in a Kratos Axis Supra DLD spectrometer equipped with a monochromatic Al K$_\alpha$ X-ray source ($h\nu = 1486.6$ eV) operating at 150 W, a multichannel plate, and a delay line detector under a vacuum of $1-10^{-9}$ mbar. The survey and high-resolution spectra were collected at fixed analyzer pass energies of 160 and 20 eV, respectively. Samples were mounted in a floating mode in order to avoid differential charging for the XPS measurements. Charge neutralization was required for all samples. Binding energies were referenced to the C 1s peak of (C−C, C−H) bond which was set at 284.8 eV. The data were analyzed with commercially available software, CasaXPS. The individual peaks were fitted by a Gaussian (70%)–Lorentzian (30%) (GL30) function after linear or Shirley-type background subtraction. UPS measurements were performed in the same instrument using a He I excitation ($h\nu = 21.22$ eV). A bias of −9 V was applied to the sample surface for UPS measurements. Samples were mounted in contact mode for the UPS measurements.

XRD Measurements: Bruker D8 Advance diffractometer was used for XRD analysis. The tool was operated at 30 kV, 10 mA at 2θ (Cu K$_\alpha$, ($\lambda = 0.15418$ nm) 30°–80°, step 0.02°, and scan speed 2.5° min^{-1}).

DFT Modeling: The Vienna Ab-initio Simulation Package[20] was used to perform the DFT calculations for an 80 atoms cell of In_2O_3 (space group: Ia$\bar{3}$, No. 206), using a cut-off energy of 500 eV and $2 \times 2 \times 2$, $4 \times 4 \times 4$, and $8 \times 8 \times 8$ k meshes for the structure relaxation, self-consistent calculation, and nonself-consistent calculation, respectively. In the structure relaxation, the Perdew–Burke–Ernzerhof[21] flavor of the generalized gradient approximation for the exchange-correlation functional was used and the Hellmann–Feynman forces to 0.01 eV Å^{-1} for all atoms were converged. To calculate the WF, In_2O_3 (100) slabs were constructed, as the most prominent peak (200) in the XRD data was corresponded to the (100) growth direction. A vacuum region of 18 Å thickness was added to separate the repeating geometries.

Spectroscopic Ellipsometry: SE measurements of the IZRO/c-Si stacks were performed by using J.A. Woollam M-2000DI at 65° and 75°. The c-Si substrate was a single-polished float-zone wafer (525 ± 25 μm) and IZRO film was deposited on the polished side. Such a substrate can effectively impede interference caused by light reflection from the rear side. An optical model of air/surface roughness/IZRO/c-Si was used to fit the (Ψ, Δ) raw data. The IZRO layer was analyzed by a combination of three oscillators: a Tauc–Lorentz oscillator, a Gaussian, and a Drude oscillator. The surface roughness was analyzed using Bruggeman effective medium approximation, composed of 50 vol% air and 50 vol% IZRO material.

Supporting Information

Supporting Information is available from the Wiley Online Library or from the author.

Conflict of Interest

The authors declare no conflict of interest.

[1] K. Yoshikawa, H. Kawasaki, W. Yoshida, T. Irie, K. Konishi, K. Nakano, T. Uto, D. Adachi, M. Kanematsu, H. Uzu, K. Yamamoto, *Nat. Energy* **2017**, *2*, 17032.

[2] NREL, Best Research-Cell Efficiency Chart, https://www.nrel.gov/pv/cell-efficiency.html (accessed: February 2019).

[3] a) D. T. Grant, K. R. Catchpole, K. J. Weber, T. P. White, *Opt. Express* **2016**, *24*, A1454; b) S. Altazin, L. Stepanova, J. Werner, B. Niesen, C. Ballif, B. Ruhstaller, *Opt. Express* **2018**, *26*, A579; c) L. G.-E. D. Forgács, D. Pérez-Del-Rey, C. Momblona, J. Werner, B. Niesen, C. Ballif, M. Sessolo, H. J. Bolink, *Adv. Energy Mater.* **2017**, *7*, 1602121; d) F. Sahli, J. Werner, B. A. Kamino, M. Bräuninger, R. Monnard, B. Paviet-Salomon, L. Barraud, L. Ding, J. J. Diaz Leon, D. Sacchetto, G. Cattaneo, M. Despeisse, M. Boccard, S. Nicolay, Q. Jeangros, B. Niesen, C. Ballif, *Nat. Mater.* **2018**, *17*, 820.

[4] F. Fu, T. Feurer, S. Pisoni, E. Avancini, C. Andres, S. Buecheler, *Nat. Energy* **2017**, *2*, 16190.

[5] a) S. De Wolf, J. Holovsky, S. J. Moon, P. Loper, B. Niesen, M. Ledinsky, F. J. Haug, J. H. Yum, C. Ballif, *J. Phys. Chem. Lett.* **2014**, *5*, 1035; b) M. Ledinsky, T. Schönfeldová, J. Holovsky, E. Aydin, Z. Hájková, L. Landová, N. Neykova, A. Fejfar, S. De Wolf, *J. Phys. Chem. Lett.* **2019**, *10*, 1368.

[6] T. K. A. M. Kondo, *J. Appl. Phys.* **2007**, *101*, 09M502.

[7] a) J. Werner, G. Dubuis, A. Walter, P. Löper, S.-J. Moon, S. Nicolay, M. Morales-Masis, S. De Wolf, B. Niesen, C. Ballif, *Sol. Energy Mater. Sol. Cells* **2015**, *141*, 407; b) K. A. Bush, A. F. Palmstrom, Z. J. Yu, M. Boccard, R. Cheacharoen, J. P. Mailoa, D. P. McMeekin, R. L. Z. Hoye, C. D. Bailie, T. Leijtens, I. M. Peters, M. C. Minichetti, N. Rolston, R. Prasanna, S. Sofia, D. Harwood, W. Ma, F. Moghadam, H. J. Snaith, T. Buonassisi, Z. C. Holman, S. F. Bent, M. D. McGehee, *Nat. Energy* **2017**, *2*, 17009; c) J. Werner, C. H. Weng, A. Walter, L. Fesquet, J. P. Seif, S. De Wolf, B. Niesen, C. Ballif, *J. Phys. Chem. Lett.* **2016**, *7*, 161.

[8] a) M. Morales-Masis, S. De Wolf, R. Woods-Robinson, J. W. Ager, C. Ballif, *Adv. Electron. Mater.* **2017**, *3*, 1600529; b) M. Chen, Z. L. Pei, X. Wang, Y. H. Yu, X. H. Liu, C. Sun, L. S. Wen, *J. Phys. D: Appl. Phys.* **2000**, *33*, 2538.

[9] T. Koida, H. Fujiwara, M. Kondo, *Jpn. J. Appl. Phys.* **2007**, *46*, L685.

[10] T. Koida, H. Fujiwara, M. Kondo, *Sol. Energy Mater. Sol. Cells* **2009**, *93*, 851.

**ADVANCED
SCIENCE NEWS**

www.advancedsciencenews.com

**ADVANCED
FUNCTIONAL
MATERIALS**

www.afm-journal.de

[11] M. Morales-Masis, S. M. D. Nicolas, J. Holovsky, S. De Wolf, C. Ballif, *IEEE J. Photovoltaics* **2015**, *5*, 1340.

[12] a) M. F. A. M. van Hest, M. S. Dabney, J. D. Perkins, D. S. Ginley, *Thin Solid Films* **2006**, *496*, 70; b) H. Ryota, A. Yoshiyuki, N. Tokio, *Appl. Phys. Express* **2008**, *1*, 015002.

[13] M. Morales-Masis, E. Rucavado, R. Monnard, L. Barraud, J. Holovský, M. Despeisse, M. Boccard, C. Ballif, *IEEE J. Photovoltaics* **2018**, *8*, 1202.

[14] H. Kim, J. S. Horwitz, G. P. Kushto, S. B. Qadri, Z. H. Kafafi, D. B. Chrisey, *Appl. Phys. Lett.* **2001**, *78*, 1050.

[15] T. Koida, M. Kondo, K. Tsutsumi, A. Sakaguchi, M. Suzuki, H. Fujiwara, *J. Appl. Phys.* **2010**, *107*, 033514.

[16] N. D. Sankir, E. Aydin, H. Unver, E. Uluer, M. Parlak, *Sol. Energy* **2013**, *95*, 21.

[17] a) E. Rucavado, Q. Jeangros, D. F. Urban, J. Holovský, Z. Remes, M. Duchamp, F. Landucci, R. E. Dunin-Borkowski, W. Körner, C. Elsässer, A. Hessler-Wyser, M. Morales-Masis, C. Ballif, *Phys. Rev. B* **2017**, *95*, 245204; b) A. J. Leenheer, J. D. Perkins, M. F. A. M. van Hest, J. J. Berry, R. P. O'Hayre, D. S. Ginley, *Phys. Rev. B* **2008**, *77*, 115215.

[18] a) S. Husein, M. Stuckelberger, B. West, L. Ding, F. Dauzou, M. Morales-Masis, M. Duchamp, Z. Holman, M. I. Bertoni, *J. Appl. Phys.* **2018**, *123*, 245102; b) N. Preissler, O. Bierwagen, A. T. Ramu, J. S. Speck, *Phys. Rev. B* **2013**, *88*, 085305.

[19] O. Bierwagen, J. S. Speck, *Appl. Phys. Lett.* **2010**, *97*, 072103.

[20] M. Marezio, *Acta Crystallogr.* **1966**, *20*, 723.

[21] Z. Chen, L. Huang, Q. Zhang, Y. Xi, R. Li, W. Li, G. Xu, H. Cheng, *J. Phys. Chem. C* **2015**, *119*, 4789.

[22] A. Seidl, A. Görling, P. Vogl, J. A. Majewski, M. Levy, *Phys. Rev. B* **1996**, *53*, 3764.

[23] a) V. Scherer, C. Janowitz, A. Krapf, H. Dwelk, D. Braun, R. Manzke, *Appl. Phys. Lett.* **2012**, *100*, 212108; b) R. L. Weiher, R. P. Ley, *J. Appl. Phys.* **1966**, *37*, 299.

[24] E. L. Runnerstrom, A. Bergerud, A. Agrawal, R. W. Johns, C. J. Dahlman, A. Singh, S. M. Selbach, D. J. Milliron, *Nano Lett.* **2016**, *16*, 3390.

[25] a) J. Stankiewicz, F. Villuendas, M. P. Lozano, I. Díez, *J. Appl. Phys.* **2013**, *114*, 083703; b) J. Gan, X. Lu, J. Wu, S. Xie, T. Zhai, M. Yu, Z. Zhang, Y. Mao, S. C. I. Wang, Y. Shen, Y. Tong, *Sci. Rep.* **2013**, *3*, 1021.

[26] H. Wardenga, M. Frischbier, M. Morales-Masis, A. Klein, *Materials* **2015**, *8*, 561.

[27] a) D. Barreca, G. A. Battiston, R. Gerbasi, E. Tondello, P. Zanella, *Surf. Sci. Spectra* **2000**, *7*, 303; b) L. Armelao, E. Tondello, L. Bigliani, G. Bottaro, *Surf. Sci. Spectra* **2001**, *8*, 268.

[28] O. Lang, C. Pettenkofer, J. F. Sánchez-Royo, A. Segura, A. Klein, W. Jaegermann, *J. Appl. Phys.* **1999**, *86*, 5687.

[29] A. Walsh, C. R. A. Catlow, *J. Mater. Chem.* **2010**, *20*, 10438.

[30] a) J. Tauc, R. Grigorovici, A. Vancu, *Phys. Status Solidi B* **2015**, *640*, 468; b) N. D. Sankir, E. Aydin, E. Ugur, M. Sankir, *J. Alloys Compd.* **2015**, *640*, 468.

[31] J. I. Pankove, *Optical Processes in Semiconductors*, Courier Corporation, North Chelmsford, MA **1975**.

[32] a) M. Balestrieri, D. Pysch, J. P. Becker, M. Hermle, W. Warta, S. W. Glunz, *Sol. Energy Mater. Sol. Cells* **2011**, *95*, 2390; b) H. Fujiwara, M. Kondo, *Phys. Rev. B* **2005**, *71*, 075109.

[33] C. Battaglia, A. Cuevas, S. De Wolf, *Energy Environ. Sci.* **2016**, *9*, 1552.

[34] a) J. Werner, L. Barraud, A. Walter, M. Bräuninger, F. Sahli, D. Sacchetto, N. Tétreault, B. Paviet-Salomon, S.-J. Moon, C. Allebé, M. Despeisse, S. Nicolay, S. D. Wolf, B. Niesen, C. Ballif, *ACS Energy Lett.* **2016**, *1*, 474; b) T. Duong, Y. Wu, H. Shen, J. Peng, X. Fu, D. Jacobs, E. Wang, T. C. Kho, K. C. Fong, M. Stocks, E. Franklin, A. Blakers, N. Zin, K. McIntosh, W. Li, Y. Cheng, T. P. White, K. Weber, K. Catchpole, *Adv. Energy Mater.* **2017**, *7*, 1700228; c) M. Jaysankar, B. A. L. Raul, J. Bastos, C. Burgess, C. Weijtens, M. Creatore, T. Aernouts, Y. Kuang, R. Gehlhaar, A. Hadipour, J. Poortmans, *ACS Energy Lett.* **2019**, *4*, 259; d) C. O. Ramirez Quiroz, Y. Shen, M. Salvador, K. Forberich, N. Schrenker, G. D. Spyropoulos, T. Huemueller, B. Wilkinson, T. Kirchartz, E. Spiecker, P. J. Verlinden, X. Zhang, M. Green, A. W. Y. Ho-Baillie, C. J. Brabec, *J. Mater. Chem. A* **2018**, *6*, 3583.

[35] a) X. Yang, E. Aydin, H. Xu, J. Kang, M. Hedhili, W. Liu, Y. Wan, J. Peng, C. Samundsett, A. Cuevas, S. De Wolf, *Adv. Energy Mater.* **2018**, *8*, 1800608; b) X. Yang, K. Weber, Z. Hameiri, S. De Wolf, *Prog. Photovoltaics* **2017**, *25*, 896.

[36] S. De Wolf, A. Descoeudres, Z. C. Holman, C. Ballif, *Green* **2012**, *2*, 7.

[37] E. Aydin, J. Troughton, M. De Bastiani, E. Ugur, M. Sajjad, A. Alzahrani, M. Neophytou, U. Schwingenschlögl, F. Laquai, D. Baran, S. De Wolf, *ACS Appl. Energy Mater.* **2018**, *1*, 6227.

[38] E. Ugur, A. D. Sheikh, R. Munir, J. I. Khan, D. Barrit, A. Amassian, F. Laquai, *ACS Energy Lett.* **2017**, *2*, 1960.

[39] X. Yang, Q. Bi, H. Ali, K. Davis, W. V. Schoenfeld, K. Weber, *Adv. Mater.* **2016**, *28*, 5891.

[40] a) J. Peng, J. I. Khan, W. Liu, E. Ugur, T. Duong, Y. Wu, H. Shen, K. Wang, H. Dang, E. Aydin, X. Yang, Y. Wan, K. J. Weber, K. R. Catchpole, F. Laquai, S. De Wolf, T. P. White, *Adv. Energy Mater.* **2018**, *8*, 1801208; b) M. De Bastiani, E. Aydin, T. Allen, D. Walter, A. Fell, J. Peng, N. Gasparini, J. Troughton, D. Baran, K. Weber, T. P. White, S. De Wolf, *Adv. Electron. Mater.* **2018**, *0*, 1800500.